Strain determination in silicon microstructures by combined TEM/CBED, process simulation and micro-Raman spectroscopy

V. Senez, A. Armigliato, I. de Wolf, G. Carnevale, R. Balboni, S. Frabboni, A. Benedetti

Strain determination in silicon microstructures by combined convergent beam electron diffraction, process simulation, and micro-Raman spectroscopy

Cite as: Journal of Applied Physics **94**, 5574 (2003); https://doi.org/10.1063/1.1611287
Submitted: 02 April 2003 • Accepted: 29 July 2003 • Published Online: 23 October 2003

Vincent Senez, Aldo Armigliato, Ingrid De Wolf, et al.

Strain determination in silicon microstructures by combined convergent beam electron diffraction, process simulation, and micro-Raman spectroscopy

Vincent Senez[a)]
IEMN–ISEN, UMR CNRS-8520, Avenue Poincaré, B.P. 69, 59652 Villeneuve d'Ascq cédex, France

Aldo Armigliato
CNR–IMM Sezione di Bologna, Via P. Gobetti 101, 40129 Bologna, Italy

Ingrid De Wolf
IMECvzw, Kalpeldreef 75, 3001 Leuven, Belgium

Gianpietro Carnevale
STMicroelectronics, via C. Olivetti 2, 20041 Agrate Brianza, Italy

Roberto Balboni
CNR–IMM Sezione di Bologna, Via P. Gobetti 101, 40129 Bologna, Italy

Stefano Frabboni
INFM–National Research Centre-S3 and Dipartimento di Fisica, Università di Modena e Reggio Emilia, via G. Campi 213/A, 41100 Modena, Italy

Alessandro Benedetti[b)]
Department of Electronic and Electrical Engineering, University of Sheffield, Mappin Street, S13JD Sheffield, United Kingdom

(Received 2 April 2003; accepted 29 July 2003)

Test structures consisting of shallow trench isolation (STI) structures are fabricated using advanced silicon (Si) technology. Different process parameters and geometrical features are implemented to investigate the residual mechanical stress in the structures. A technology computer aided design homemade tool, IMPACT, is upgraded and optimized to yield strain fields in deep submicron complementary metal–oxide–semiconductor devices. Residual strain in the silicon substrate is measured with micro-Raman spectroscopy (μ-RS) and/or convergent beam electron diffraction (CBED) for large (25 μm) and medium size (2 μm), while only CBED is used for deep submicron STI (0.22 μm). We propose a methodology combining CBED and technology computer aided design (TCAD) with μ-RS to assess the accuracy of the CBED measurements and TCAD calculations on the widest structures. The method is extended to measure (by CBED) and calculate (by TCAD) the strain tensor in the smallest structures, out of the reach of the μ-RS technique. The capability of determining, by both measurement and calculation, the strain field distribution in the active regions of deep submicron devices is demonstrated. In particular, it is found that for these structures an elastoplastic model for Si relaxation must be assumed. © *2003 American Institute of Physics.* [DOI: 10.1063/1.1611287]

I. INTRODUCTION

As the scaling and the complexity of electronic devices increase, mechanical stress/strain issues are becoming more and more relevant for the functionality of the whole device. To understand how stresses occur during silicon processing, what are the damage mechanisms, and how to control them, it is necessary to correlate the design of submicron test structures with the characterization of stresses in silicon, the study of thin film mechanical properties, and with the modeling/simulation of these problems. This is one of the current challenges for the semiconductor industries.

Nowadays, one of the best-known methods for measuring local process-induced mechanical strains in Si at micron dimensions is micro-Raman spectroscopy. This technique was applied to integrated circuit processing at the end of 1980[1,2] for the measurement of stress induced by local oxidation of silicon (LOCOS)[3] in the Si substrate. After these first reports, the technique rapidly found its way into the semiconductor research centers and microelectronics industry for stress measurements near nitride and oxide stripes, LOCOS and alternative LOCOS such as polybuffered local oxidation of silicon (PBLOCOS or LOPOS)[4] and polysilicon encapsulated local oxidation (PELOX),[5] deep and shallow trenches, near metal and silicide lines, in silicon–germanium (Si–Ge) films and even in microelectromechanical systems (MEMS) and complete Si chips.[6–9] Although the technique is relatively simple and offers fast qualitative information on

a)Now with LIMMS/CNRS-IIS, Institute of Industrial Science, The University of Tokyo, 4-6-1 Komaba, Meguro-ku, Tokyo 153-8505 Japan; electronic mail: vsenez@iis.u-tokyo.ac.jp
b)Now at IMECvzw, Kapeldreef 75, 3001 Leuven, Belgium.

local stress, it has two partial drawbacks. The spatial resolution of a conventional system is limited to about 1 μm and one has to start from analytical or finite element models if the different stress/strain tensor components have to be obtained. Many studies have be performed in order to increase the spatial resolution, the most important being the use of solid immersion lenses (SIL), pioneered by Poweleit and Menendez,[10] and the adaptation of near-field scanning optical microscopy (NSOM) for spectroscopy.[11] The latter is still limited by the very small throughput of incident and collected light: low intensity Raman signals can be obtained but only when using relatively large tip apertures (150–200 nm).[12–14] These signals are too small to be really useful for stress measurements. SIL promises to be a good alternative, but there is still a significant gap between the demonstrated possibilities of these lenses and their practical application to Raman spectroscopy.

However, for very advanced complementary metal–oxide–semiconductor (CMOS) devices, the spatial resolution given currently by micro-Raman spectroscopy (μ-RS) is not sufficient. The only technique that can provide information on lattice strain with a higher spatial resolution is the convergent beam diffraction technique of transmission electron microscopy (TEM). It is a well-established technique for the point-to-point determination of strain in a thin film.[15,16] This technique has been widely used in the last years to study unpatterned structures such as Si–Ge/Si heterostructures.[17–20] The application of TEM/convergent beam electron diffraction (TEM/CBED) to the determination of local strains in microelectronic devices started about one decade ago. Micron-sized LOCOS structures were first investigated;[21–23] and more recently, with the advent of the shallow trench isolation (STI) structures, the technique has been applied to deep submicron Si active regions.[24–27] The availability of microscopes equipped with field emission guns (FEGs) (FEG/TEM) has enabled the achievement of a spatial resolution at the nanometer scale.[24,27]

The coupling of these experimental techniques with numerical analysis is necessary and valuable. It allows us to optimize and to validate the numerical analysis. The latter is essential for the development of integrated circuits (ICs). Indeed, with technology computer aided design (TCAD), one can test, at low development time and cost, many modifications of the process flow both in terms of process conditions and/or device geometries to define the state-of-the-art technology with respect to stress.

One can consider the birth of TCAD contemporary to those of integrated circuits with the first pioneering works of Gummel, Scharfetter, Deal, and Grove[28–30] about the modeling of the bipolar transistor and of the oxidation of Si. At the beginning of the 1980's, numerical implementation of simple models allowing one-dimensional (1D) or two-dimensional (2D) analysis of the electrical behavior of transistors[31,32] or of the microfabrication of integrated components[33–35] are already available. With the growing power of computers and the spreading of TCAD in the IC industry, the number of 2D codes grew quickly[36–40] and three-dimensional (3D) solutions appeared in the 1990's.[41–44] For the simulation of the microfabrication steps (i.e., lithography, deposition, etching, diffusion, oxidation, silicidation, etc.), the role of TCAD is to predict the morphology of the device as well as the distributions of doping and mechanical stresses/strains in all materials during each step. Historically, the first works have concentrated on the prediction of the morphology and doping distributions, which explains why the models are currently more advanced on these aspects than on mechanical ones. Even if stress problems in Si technologies were very early the topic of many investigations, most of them were studied only using analytical modeling or general purpose finite element (FE) software.[45–47] Calculations of stresses in TCAD were first introduced for the modeling of Si oxidation.[48–53] With the improvements in the Si technologies, the other sources of stresses and their effects became also a topic of great interest for TCAD.[54–56] First, TCAD tools giving the possibility to calculate the distribution of mechanical stresses/strains in all materials during all process steps appeared in the beginning of the 1990's.[57,58] The calibration of the mechanical parameters appearing in the various numerical models was obtained either by an indirect measurement of stress effects (e.g., on SiO_2 growth or doping diffusion) or by using the wafer curvature technique.[59] Currently, with microdevices having typical dimensions close to 100 nm, these calibration methodologies are not adapted. To further improve the reliability of the numerical stress models, we need to validate the calculations with direct (i.e., using μ-RS or CBED) measurements of stress or strain in microstructures.

II. EXPERIMENT

A. Fabrication of STI structures

Shallow trench isolation is one of the most critical technology modules from the point of view of stress generation in the silicon substrate. In fact, as widely reported in the literature, several process parameters related to this module can be strictly correlated with defect generation and, therefore, with active device electrical behavior.[60,61] Samples have been prepared on 8 in., *p*-type silicon wafers with ⟨100⟩ orientation. The STI fabrication starts with the growth of a silicon oxide thin film on bare silicon; on top of this film a thick silicon nitride layer is deposited at the temperature of 775 °C and in the range of 120–160 nm thickness. The stack is then exposed and patterned: the silicon active areas are masked by resist and the nitride/oxide stack itself, while a trench is etched by means of a reactive ion etching (RIE). Then, a thermal oxide is grown at high temperature on the trench walls. Depending on the process conditions of this oxidation step that can be optimized in order to remove the plasma damage, a facet can be generated at the bottom corner of the trench. Different oxide deposition techniques can then be used for filling of the isolation region. A possible solution is based on a sequence of two deposition steps: the first film is a high density plasma (HDP) oxide for a thickness of 400 nm at an estimated temperature of 300 °C, while the second oxide layer is obtained by a low pressure chemical vapor deposition (LPCVD) technique with tetra-ethoxysilane (TEOS) reactant and is deposited for a thickness of about 500 nm at a temperature of 700 °C.[62,63] Figure 1 shows a transmission electron microscope view of the 2-μm-wide structure after

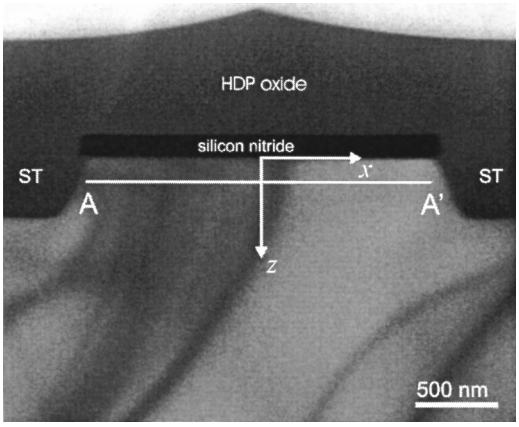

FIG. 1. Cross-sectional TEM picture of the 2 μm structure, taken after the filling of the shallow trenches (ST) with the LPCVD-TEOS and HDP films. The 160 nm silicon nitride film is labeled, whereas the thin padoxide layer is hardly visible at this low magnification. The coordinate axes x ($[-1,1,0]$) and z ($[001]$) are shown, together with the $z=100$ nm A-A' cutline analyzed by the CBED technique (see Fig. 9). Note that the strain analysis is always performed in the crystallographic system of coordinates X ($[100]$), Y ($[010]$), and $Z=z$ ($[001]$).

the filling step. Another option is to use for the filling of the trench a deposition of two HDP oxide films with different deposition/sputter etching ratios. A thermal treatment consisting of an inert annealing at a temperature higher than 1000 °C is required in order to reflow the deposited filling oxide and to bring its density and the mechanical properties close to those of the thermal oxide. Finally, the structure is planarized by a chemical–mechanical polishing (CMP) step. Before removing the nitride film by a phosphoric acid solution, the oxide is recessed with respect to the nitride by a wet etch. Figure 2 shows a scanning electron microscope view of the 2-μm-wide structure after the CMP step. Two process splits have been implemented: the first one is concerned with the thickness of the nitride film (120 or 160 nm), whereas in the second the filling of the oxide trench is varied (HDP with TEOS or full HDP).

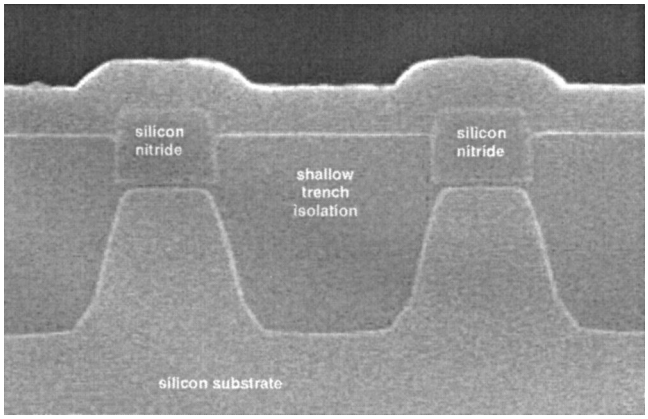

FIG. 2. SEM picture of the sample after the CMP operation and the wet etch of STI oxide; the above top layer is a polysilicon film deposited in order to improve the image contrast, which covers the nitride stack over the silicon active area and the HDP oxide used to fill the silicon trench (darker region in the SEM picture).

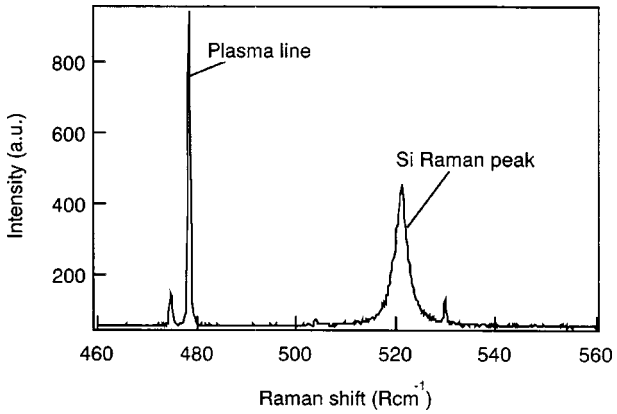

FIG. 3. Raman spectrum of crystalline silicon, measured using the 457.8 nm line of an argon laser. It shows the Si Raman peak and plasma lines from the laser.

Measurements have been performed before the densification treatment by means of both the CBED and the micro-Raman spectroscopy technique on different structures: 25.0 μm active area with pitches of 30 μm, 2.0 μm active area with pitches of 4.0–8.0 μm and 0.22 μm active area with a pitch of 0.7 μm.

B. Micro-Raman spectroscopy

The 458 nm light (blue) of an argon laser is used for the Raman experiments. This light is focused through a microscope on the sample, giving a probing spot diameter of about 0.8 μm. The sample is mounted on an automated XY stage under the microscope such that Raman spectra can be recorded at different positions along a line on the sample, with steps as small as 0.1 μm. Figure 3 shows a typical Raman spectrum of crystalline Si. The frequency of the Si Raman peak depends on mechanical stress. In order to determine this frequency, the peak is fitted with a Lorentzian function. The plasma lines of the laser are used as reference. Their frequency is not influenced by stress in the Si. They are fitted using a Gaussian function to determine their frequency. Variations in the position of the plasma line are due to instrumental variations (laser, room temperature, detector temperature, etc.). The Raman spectra are corrected for these variations using the plasma lines.

The relation between the strain tensor components and the Raman frequency can be obtained by solving the secular equation.[64] In general, this gives rather complex relations. They become very simple if one assumes uniaxial stress, σ, in the Si. The relation between the shift of the Si Raman peak frequency as measured on the (100) surface of a wafer and this stress is then given by

$$\sigma \ \ (\mathrm{MPa}) = -434\Delta\omega \ \ (\mathrm{cm}^{-1}). \tag{1}$$

For biaxial stress, the relation between the Raman shift and the stress is given by

$$\sigma_{xx}+\sigma_{yy} \ \ (\mathrm{MPa}) = -434\Delta\omega \ \ (\mathrm{cm}^{-1}). \tag{2}$$

So, if tensile stress is present ($\sigma>0$), the Si Raman frequency will shift downwards ($\Delta\omega<0$), whereas for compressive stress ($\sigma<0$), it will shift upwards ($\Delta\omega>0$).

For more complicated stress distributions, the relation between the stress tensor components and the measured Raman shift is not so straightforward, and special modeling is necessary if quantitative stress values are required. Using the stress data obtained from our TCAD tool (see Sec. III), the ''theoretically expected'' Raman frequency shift was calculated and then compared to the Raman spectroscopy measurements. Finally, since the CBED technique provides direct quantitative information on the strain tensor components, we have used these data to calculate the corresponding Raman shift, thus allowing a direct comparison between CBED and Raman spectroscopy measurements.

C. CBED analysis

The CBED technique for strain measurement is based on the strain induced shift of high order Laue zone (HOLZ) deficiency lines.[65] They occur in the central disk of a CBED pattern when the incident electron beam has a suitable convergence (typically of the order of 10 mrad) and is aligned parallel to a zone axis. Due to their high-angle scattering origin, the position of these lines is very sensitive, among other parameters, to small variations in acceleration voltage and lattice parameters, and therefore to strain. In particular, strains of the order of 2×10^{-4} can be detected by HOLZ line shifts. In order to quantify the strain, it is first necessary to assess the effective acceleration voltage by matching, through a χ^2-based minimization procedure, the pattern taken on the unstrained part of the sample with a kinematically simulated one. Then, the unknown lattice parameters are determined by fitting the experimental pattern taken on the strained layer with a simulated one, assuming the lattice constants as fitting parameters.

In principle, all six lattice parameters $(a,b,c,\alpha,\beta,\gamma)$ can be deduced from a single CBED pattern. However, it is presently impossible to get a unique solution keeping all these parameters free.

This difficulty can be overcome when the crystal symmetry allows us to reduce the total number of independent parameters to be determined, as in the case of the STI devices investigated in this article, which are patterned along the [110] direction. In such samples, all the stress sources lie in a plane perpendicular to this crystallographic direction. It can then be easily demonstrated that the distortions applied along the crystallographic directions X ([100]) and Y ([010]) are the same, since they both form angles of 45° with the [110] direction: hence, $a=b$. The problem of stress relaxation in a specimen thinned for TEM observation must be also considered; this occurs mainly at the surfaces of the cross-sectioned sample, which consist of regions with strain gradients. A good quality CBED pattern can be obtained only if a sufficiently large, homogeneously strained volume of crystal is probed by the electron beam: this ''bulk'' region increases with the specimen thickness. Then, as a general rule, if a good quality (analyzable) pattern is recorded in sufficiently thick specimens (200–300 nm at 200 kV), it can be concluded that in that region the strain relaxation, although present, can be neglected.

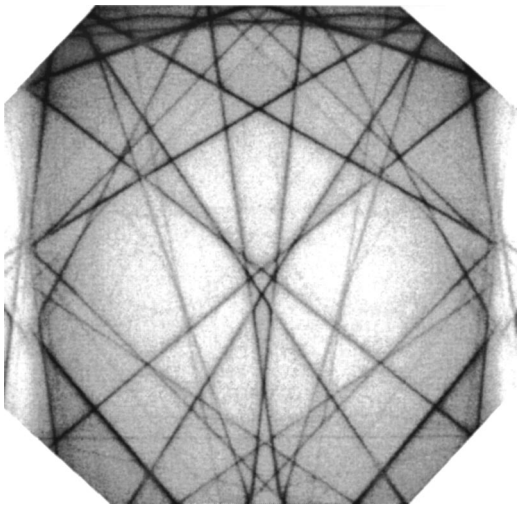

FIG. 4. Experimental CBED pattern taken in undeformed silicon. Zone axis: ⟨230⟩; acceleration voltage: 200 kV. A set of sharp HOLZ lines is clearly visible in this enlarged view of the central disk of the pattern.

This assumption, the so-called plane strain approximation, leads to a further reduction of the number of unknowns to be determined. It can be easily demonstrated by imposing that there is no stress relaxation along the thinning direction [110], the angle γ and the parameters $a=b$ are mutually dependent and follow the relation:[66]

$$\frac{\Delta a}{a}=\frac{\Delta b}{b}=\frac{\Delta\gamma/2}{1-\Delta\gamma/2}\approx\frac{\Delta\gamma}{2}.$$

Moreover, by taking into account that the deformations analyzed in these devices are generally small, it can be assumed that $\alpha=\pi-\beta$, which implies that $\epsilon_{XZ}=-\epsilon_{YZ}$. In this way, the number of independent parameters to be determined is reduced from 6 to 3 (a, c, and α); this generally results in a unique sharp minimum in the χ^2 plots.

To determine by CBED the strain field distribution in the STI structures investigated in this work (Figs. 1 and 2), cross-sectional samples have been prepared by mechanical lapping down to 20 μm and then by ion beam milling to performation. They have been analyzed by a field emission transmission electron microscope, using a spot size of 1 nm. The CBED patterns were taken in the ⟨230⟩ orientation, which is 11.3° off the vertical ⟨110⟩ direction, at an accelerating voltage of 200 kV. An example of a pattern, taken in an undeformed Si area of a cross section, is shown in Fig. 4; the HOLZ deficiency lines appear as a set of straight lines, whose position in the pattern is related to the local values of the lattice parameters of the Si cell.

III. PROCESS SIMULATOR IMPACT

A. Mechanical models

The mechanical stress which develops in integrated devices during their fabrication is affected by six components: (i) temperature change, (ii) thermal growth of material [i.e., silicon dioxide (SiO_2) and silicides], (iii) etching of materials, (iv) deposition processes which create intrinsic stresses, (v) implantation of doping ions, and (vi) structural changes

of deposited films due to densification, hydration/dehydration, and crystallization. These phenomena generate a loss in the mechanical equilibrium of the system composed of the Si substrate with a stack of thin film layers on top (i.e., the microelectronic device). These mechanical solicitations can always be expressed as a mechanical strain load using macroscopic modeling of the phenomena (e.g., Deal and Grove's model for thermal growth, Vegard's law for implantation, Fick's equation for evaporation or absorption of water, etc.). Knowing the initial load and the residual stress due to previous process steps, we calculate the new distribution of the internal stress applying the equilibrium conditions for the forces. For the accuracy of the calculations, we take into account the complex thermomechanical thin film properties. In the range of temperatures used in the front-end processes ([700–1100 °C]), and in the range of stresses measured in thin film materials ([20 MPa–2 GPa]), microelectronics materials show very different mechanical behaviors, from elastic (e.g., Si) to viscous (e.g., highly stressed SiO_2 at high temperature). Furthermore, at these temperatures and/or stress levels, the amorphous materials may exhibit viscoelastic behaviors[67] and the (poly)-crystalline materials may have elastoplastic behaviors.[68] Simple macroscopic rheological models (i.e., Hook's, Saint Venant's, Maxwell's, Newton's laws) are available in the literature to represent all of these mechanical properties.

B. Numerical implementation

Stress models have been developed for the following materials: silicon, polysilicon, tetra-ethoxysilane, silicon dioxide (SiO_2), HDP–SiO_2, phosphosilicate glass (PSG), borophosphosilicate glass (BPSG), thermal SiO_2, Si_3N_4 deposited by LPCVD or plasma enhanced chemical vapor deposition (PECVD), titanium and cobalt thermal silicides, tungsten, aluminum, copper, cobalt, and titanium. In Si, the anisotropy of the mechanical properties has also been incorporated. The Si substrate is considered free of stress and strain at the beginning of all process simulations. The equations of these mechanical models have been implemented in our homemade 2D process simulator, IMPACT.[69–71] The IMPACT software is a multidimensional platform allowing from the process and layout description of an integrated circuit to define input files for 1D and 2D processes. IMPACT allows other process simulators to be plugged in rather easily and it is interfaced to device simulation.

In this software, we have adopted the FE method using the Galerkin weighted residual formulation for the solution of the equilibrium equations. The initial mesh is a Delaunay triangular one. We use a single mesh for all species, and linear shape functions have been chosen to approximate the real stresses and strains. The general iterative treatment of the mechanics for a processing step is given in Ref. 67.

C. Simulation of the STI structure

To determine by calculation the strain field distribution in the STI structures investigated in this work (Figs. 1 and 2), we have used the symmetry of the structure and defined an initial simulation domain, composed of one material (i.e., Si), being half the active and isolation area width and 10 μm thick. Then, the following processing steps have been simulated: pad oxide (padox) formation, nitride deposition, annealing of oxidation mask, etching of nitride, and padox to define the active area, etching of Si to define the trench, ramp up, dry oxidation of the trench and annealing, ramp down, and finally, filling of the trench with either HDP or HDP +LPCVD-TEOS. All these steps contribute to the generation of strain in the Si substrate. Figure 5 gives the simulated morphology of this STI structure. One should note the presence of a compressive peak at the center of the active area, induced by the intrinsic tensile stress of the nitride layer. One can also see the appearance of a high tensile peak at the tip of the bird's beak and of a high compressive peak at the top Si corner due to oxide growth on a convex angle. The opposite behavior is generally observed at the bottom Si corner (i.e., tensile peak due to oxide growth on a concave corner), but which is much reduced here due to the faceting of the corner.

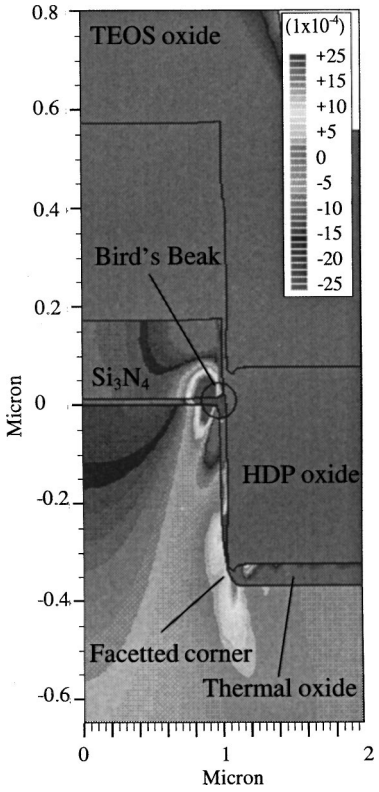

FIG. 5. 2D distributions of the trace of the strain tensor in the STI structure before the densification of the HDP/TEOS oxides. Tensile peaks ($+25\times10^{-4}$) are located at the tip of the bird's beak and at the bottom corner of the shallow trench. A compressive peak (-25×10^{-4}) is observed at the top corner of the active area.

IV. RESULTS AND DISCUSSION

A. 25.0- and 2.0-μm-wide STI structures

The above outlined procedures have been applied to determine the strain in the STI structures shown in Fig. 1. Raman spectroscopy experiments were performed across 2.0- and 25.0-μm-wide active lines isolated by shallow trenches, as shown in Fig. 6. The Raman frequency of the Si

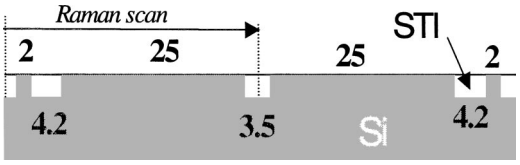

FIG. 6. Schematic picture of the sample used for Raman spectroscopy experiments. It consists of 2- and 25-μm-wide Si lines isolated by shallow trenches (STI). The arrow indicates the region scanned by Raman spectroscopy. It crosses first a 2-μm-wide Si line and next a 25-μm-Si line. The results of this measurement are shown in Fig. 7.

peak is measured during a scan across these structures. We first discuss the results for the 25.0 μm line. As can be seen in Fig. 7, a negative Raman frequency shift (negative $\Delta\omega$) is measured just outside the edges of the active area, indicating tensile stress. This stress might be present either in the Si at the vertical wall of the active region that is in contact with the oxide, or just at the edge in the Si underneath the isolation. The resolution of the technique is not good enough to make any conclusions on this. Compressive stress is seen at the edge of the active area (positive $\Delta\omega$), fast decreasing away from the edge towards the center of the active area. For the 2.0-μm-wide active line (left part of the curve in Fig. 7), the picture is somewhat different. The compressive stresses present at the right and left edge of the active area, as observed in the 25.0 μm active line, now overlap giving rise to a compressive stress in this narrow line which is larger than the one seen at the edge of the wide line. The tensile stress near the edges (negative $\Delta\omega$) is smaller in this structure. In order to obtain quantitative data on these stresses, the Raman spectroscopy results are compared with CBED and/or FE data.

μ-RS emulation[64] has been implemented in IMPACT in order to convert the calculated stress tensors into Raman frequency shifts. Figure 8 presents the evolution of the calculated and measured Raman shift as a function of the lateral position for the 2.0 μm active line. For the simulations, we have assumed that Si behaves elastically while SiO_2 and Si_3N_4 are viscoelastic materials. One can see that the calculations can predict accurately the variation of the stress in these structures. The agreement is worse around the trench wall where several tensile and compressive peaks are located at the same x coordinate. Indeed, since the absorption depth of the laser used in μRS is around the depth of the trench, all these peaks are integrated in the Raman signal. The missing

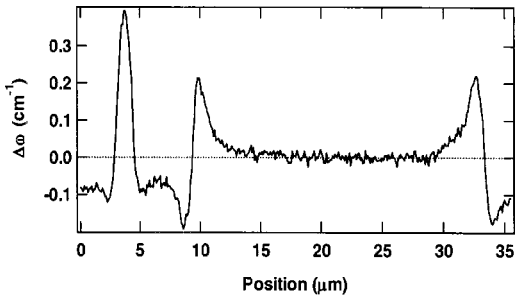

FIG. 7. Raman frequency shift measured during a scan across the structure shown in Fig. 6.

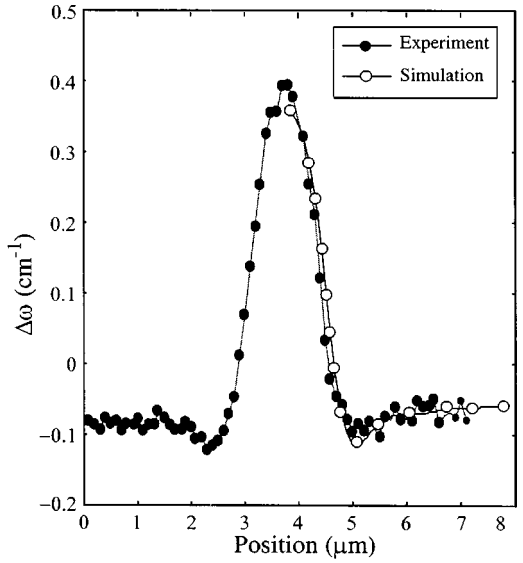

FIG. 8. Calculated and measured Raman frequency shift as a function of the lateral position in the 2-μm-wide device of the structure shown in Fig. 6.

information on the vertical gradient of the stress in these STI structures can be obtained through the CBED technique.

A number of CBED patterns have been taken along a line parallel to the padoxide/substrate interface in the active regions of the 2-μm-wide structure (AA' cutline in Fig. 1). Figure 9 shows the plots of the strain distributions obtained along this cutline taken at a depth $z=100$ nm below the pad oxide/substrate interface. The three independent components

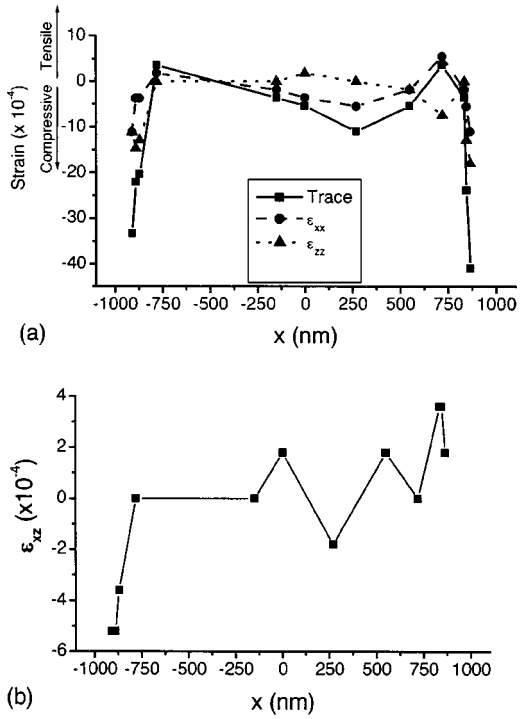

FIG. 9. Components of the strain tensor in the 2 μm STI structure along the AA' line in Fig. 1 (cut line at $z=100$ nm), as obtained from the CBED analysis. (a) Diagonal components and trace of the tensor; (b) XZ shear strain component. The trace is symmetric with respect to the center of the structure, whereas the shear strain is asymmetric, as expected.

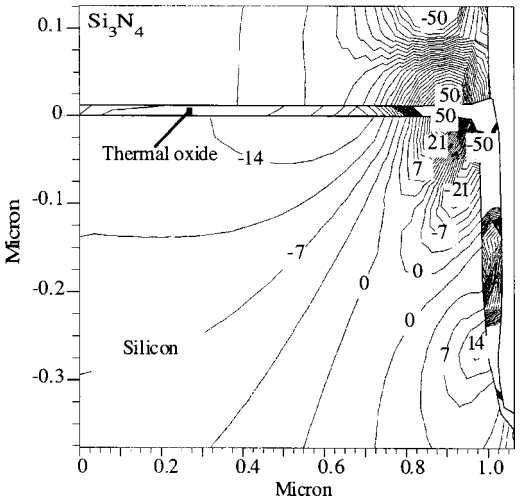

FIG. 10. 2D calculated distribution of the trace of the strain tensor in the 2-μm-device of the structure shown in Fig. 6. Strain values are divided by 1×10^{-4}.

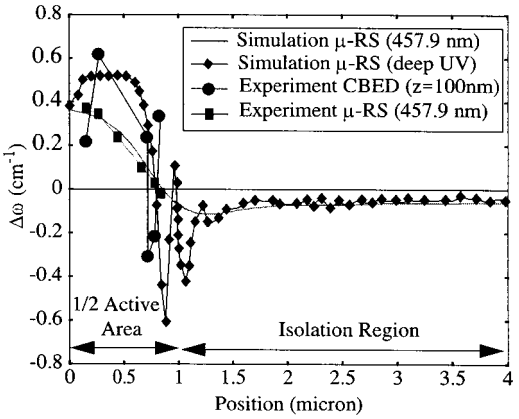

FIG. 12. Comparison between the Raman shifts obtained from: (1) simulated μRS experiment (457.9 nm, no symbol), (2) simulated μRS experiment (deep UV, diamond), (3) CBED experiment (cut line at $z=100$ nm under the Si/SiO_2 interface, circle), and (4) real μRS experiment (457.9 nm, square) in the 2-μm-wide STI structure.

of the strain tensor ($\epsilon_{XX}=\epsilon_{YY}$, ϵ_{ZZ}, and $\epsilon_{XZ}=-\epsilon_{YZ}$) are shown, together with the trace of the tensor $[\mathrm{Tr}(\epsilon)=\epsilon_{XX}+\epsilon_{YY}+\epsilon_{ZZ}=2\epsilon_{XX}+\epsilon_{ZZ}]$. This last parameter, which represents the local volume variation of the unit cell, has proved to be more useful than the single strain components in the comparison between the CBED values and those computed by the IMPACT process simulator. It is evident that the trace is generally negative, which indicates a compressive strain; it is more marked at the edges of the active regions (i.e., closer to the trenches).

Figure 10 gives the calculated 2D distribution of the trace of the strain tensor for the corresponding structures. If we compare these calculations with the measurements presented above (Fig. 11), the agreement is pretty good, bearing in mind that, according to the simulation (Fig. 10), within this Si region the distribution of the strain is expected to be very complex, showing large gradients.

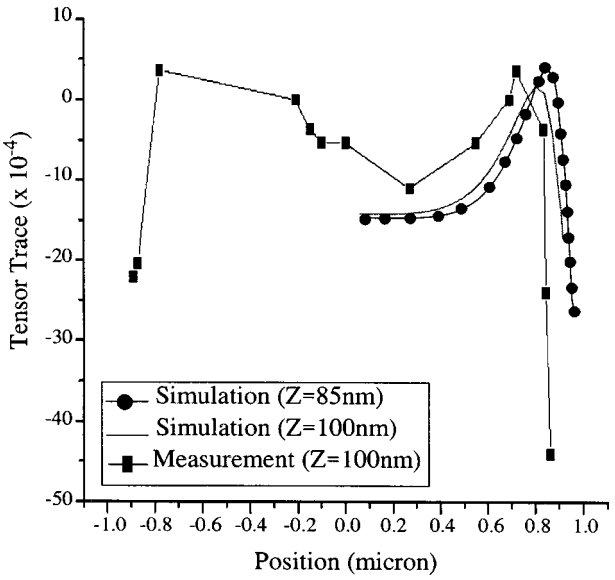

FIG. 11. Comparison between the calculated and measured trace of the strain tensor as a function of the lateral position in the 2-μm-wide STI structure along a cut line at $z=100$ nm below the silicon/silicon dioxide interface. The numerical calculations are performed with an elastic model of the rheological behavior of silicon.

In order to assess the results given by both the CBED measurements and the FEM calculations, we compare them to the measurements performed with μRS. For this purpose, we have converted the data given by the CBED technique (i.e., the strain components) into Raman shifts. From CBED measurements, the values of the three strain components are obtained at different positions along the structures and at different depths. These values are filled into the secular equation,[64] and this equation is then solved for eigenvalues and eigenvectors. From these values, the Raman frequency shift and intensity can be calculated. This allows a direct comparison of CBED data and Raman spectroscopy data. The results from this ''CBED to Raman'' conversion are compared to the measured Raman spectroscopy data in Fig. 12. We observed some discrepancies between these two types of experimental data, in terms of magnitude as well as variation along the x coordinate. The CBED data (solid circles in Fig. 12) show a reduction of the compressive peak in the center of the active area while the measurements obtained by μRS (solid squares in Fig. 12) do not show this. Both measurements exhibit a reduction of the compressive peak towards the border of the active area. The CBED measurements show also a second, smaller, compressive peak at the edge of the active area while this peak is not observed in the μRS data. There are two reasons for these discrepancies. First, Raman spectroscopy measures a weighted value with depth, while CBED does not. Second, Raman spectroscopy has a spot size of about 1 μm while CBED had a much smaller spot size. The calculations of the Raman shifts from the simulated stress tensors taking into account the properties (i.e., beam diameter and depth of absorption) of the 457.9 nm argon laser (solid line in Fig. 12) show a good agreement with the Raman measurements. If we perform the same calculations but considering an extremely small depth of absorption (100 nm) and an extremely small diameter of the laser beam (20 nm), one can observe an even better agree-

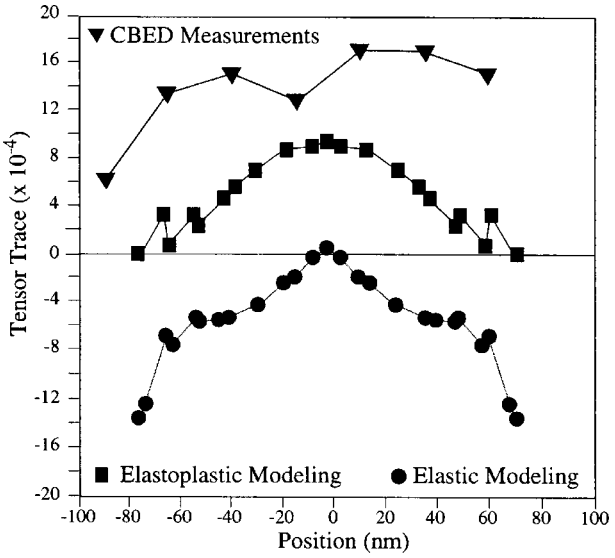

FIG. 13. Comparison between the calculated and measured trace of the strain tensor as a function of the lateral position in the 0.22-μm-wide STI structure along a cut line at $z=100$ nm below the silicon/silicon dioxide interface. The center of the active area is located at $x=0$ nm. Numerical calculations are performed either with an elastic (circle) or elastoplastic (square) model of the rheological behavior of silicon.

ment between the Raman shifts obtained from the CBED data and these simulations (solid squares in Fig. 12). In particular, the simulations show the reduction of the compressive peak at the center of the active area and the appearance of a second compressive peak at its edge. This result is interesting for three reasons: (i) it shows that both techniques give the same information, (ii) the numerical model is able to predict the fine details measured by the CBED technique, and (iii) Raman spectroscopy measurements using the so-called ''deep UV Raman'' technique, giving a smaller penetration depth and smaller spot size, would open, when available, perspectives for stress measurements using Raman spectroscopy.

B. 0.22-μm-wide STI structure

For these very compact structures, μRS could not be used since we are far from its best spatial resolution. The CBED technique is the only choice, although the measurement and its comparison with the calculations are rather difficult to carry out due to the extremely large strain gradient in this compact structure and due to the uncertainty in the localization of the probed region of the sample (about ± 20 nm diam, due to projection effects in the $\langle 230 \rangle$ orientation). According to the simulations performed on the 2-μm-wide structure, we expected to find a tensile state of strain at the center of the active area. Indeed, the calculated tensile stresses present at the right and left edges of the 2-μm-wide active area (Figs. 5 and 10) should overlap in the 0.22 μm active line. However, the first calculations predict a compressive state of strain in this area as well as unrealistic stress levels (>2 GPa) in the top corner of the active area (solid circles in Fig. 13). This means that for very compact structures, we overestimate the amount of energy stored in the active area using elastic modeling for the mechanical behavior of Si. As a consequence, the distribution of the strain is completely modified in this area and, expectedly, does not match the results given by the CBED technique (solid triangles in Fig. 13). Therefore, we have performed the calculations introducing an elastoplastic model for Si (solid squares in Fig. 13). We have only considered an isotropic plasticity criterion, the von Mises criterion.[72] It is very similar to the Tresca criterion[73,74] but has as an advantage that it is continuous, which is better for numerical implementation. In the simulation, this yield stress is fixed at 1.5 GPa. Thanks to the work performed on the 2-μm-wide structure assessing the accuracy of the CBED measurements and FEM calculations against the well-established μRS, we can conclude that it is mandatory to use elastoplastic modeling for Si in mechanical analysis of deep submicron structures involving thermal oxidation of Si. However, for the most compact structures, the comparison between calculated and measured results is presently difficult. Indeed, in these small active areas, the gradient of the strain is much more important ($>$8e-4/nm) than in the 2-μm-wide structure and the errors on the location of the measure (about 20 nm) are nonnegligible compared to the size of the active area. Methodological developments of the CBED procedure for strain analysis are presently in progress to overcome these difficulties. They include (i) the investigation of zone axes with reduced sample tilt angles ($<10°$), which will reduce the probed volume at each point, and (ii) the measurement of 2D strain maps through a digital beam positioning and a faster procedure for the extraction of the strain tensor. The comparison between experimental and simulated 2D strain maps would allow in the near future a better assessment of the accuracy of the models.

V. CONCLUSIONS

Strain data have been measured in test structures consisting of a few microns and submicron wide STI devices. For the widest structures, the measurement was made using both μRS and CBED techniques, while for the narrowest one, only CBED was performed. These data were used to assess the accuracy of numerical models implemented in a TCAD software (IMPACT). On the other hand, the numerical simulation was useful for the measurements by understanding how the strain is built in Si during the process and providing all components of the strain tensor. In particular, for the 2-μm-wide structure, we could show that (i) CBED and μRS measurements see the same strain in the STI structures and (ii) the numerical simulation can predict this strain. We have converted the CBED and calculated strain components into Raman shifts to perform the comparison. Thanks to the agreement obtained on the widest structure, we could rely on the CBED data obtained for the narrowest one, and thus compare it with the calculations. This comparison has shown the necessity to model Si as an elastoplastic body. This important result demonstrates that now a powerful tool is available to assess the state-of-the-art technology with respect to stress in terms of both reliability and stress-carrier mobility coupling. Its benefits lie in accelerating technology development, process integration/optimization, and substantially re-

ducing time to market. The future work will address the crucial issue of establishing a direct link between the stress state obtained by process simulation and the electrical failures observed in the devices.

ACKNOWLEDGMENTS

This project has been carried out within STREAM Project No. IST-1999-10341, funded by the EU. The authors would like to acknowledge the contributions of all STREAM partners: Thomas Hoffmann (IEMN), G. Pavia, P. Colpani, G. Mastracchio (ST Microelectronics), T. Schilling (Soft Imaging System—SIS), A. G. Cullis (University of Sheffield), and G. Carlotti (University of Perugia).

[1] K. Kobayashi, Y. Inoue, T. Nishimura, T. Nishioka, H. Arima, M. Hirayama, and T. Matsukawa, Extended Abstracts of the 19th Conference on Solid State Device Materials, Tokyo, Japan (1987), p. 323.
[2] H. Brunner, G. Abstreiter, B. O. Kolbesen, and H. W. Meul, Appl. Surf. Sci. **39**, 116 (1989).
[3] J. A. Appels, E. Kooi, M. M. Paffen, J. J. H. Schatorje, and W. H. Verkuyle, Philips Res. Rep. **25**, 118 (1970).
[4] M. Ghezzo, E. Kaminsky, Y. Nissan-Cohen, P. Frank, and R. Saia, J. Electrochem. Soc. **136**, 1992 (1989).
[5] S. Roth, W. Ray, C. Mazure, and H. Kirsch, IEEE Electron Device Lett. **12**, 92 (1991).
[6] I. De Wolf and H. E. Maes, Microsyst. Technol. **5**, 13 (1998).
[7] I. De Wolf, J. Raman Spectrosc. **30**, 877 (1999).
[8] I. De Wolf, C. Jian, and W. M. van Spengen, Opt. Lasers Eng. **36**, 213 (2001).
[9] F. Meyer, M. Zafrany, M. Eizenberg, R. Beserman, C. Schwebel, and C. Pellet, J. Appl. Phys. **70**, 4268 (1991).
[10] C. D. Poweleit, A. Gunther, S. Goodnick, and J. Menéndez, Appl. Phys. Lett. **73**, 2275 (1998).
[11] E. Betzig and J. K. Trautman, Science **257**, 189 (1992).
[12] C. L. Jahncke, M. A. Paesler, and H. D. Hallen, Appl. Phys. Lett. **67**, 2483 (1995).
[13] S. Webster, D. N. Batchelder, and D. A. Smith, Appl. Phys. Lett. **72**, 1478 (1998).
[14] T. A. Milster, F. Bailey, M. Erwin, J. K. Felix, D. M. Hirota, K. Koester, S. Shimura, and K. Zhang, Jpn. J. Appl. Phys., Part 1 **40**, 1778 (2001).
[15] J. W. Steeds, in *Introduction to Analytical Electron Microscopy*, edited by J. J. Hren, J. I. Goldstein, and D. C. Joy (Plenum, New York, 1979), p. 387.
[16] J. C. H. Spence and J. M. Zuo, *Electron Microdiffraction* (Plenum, New York, 1992).
[17] D. J. Eaglesham, D. M. Maher, H. L. Fraser, C. J. Humphreys, and J. C. Bean, Appl. Phys. Lett. **54**, 222 (1989).
[18] D. Cherns, R. Touatia, A. R. Preston, C. J. Roussouw, and D. C. Houghton, Philos. Mag. A **64**, 597 (1991).
[19] A. Armigliato, M. Servidori, F. Cembali, R. Fabbri, R. Rosa, F. Corticelli, D. Govoni, A. V. Drigo, M. Mazzer, F. Romanato, S. Frabboni, R. Balboni, S. S. Iyer, and A. Guerrieri, Microsc. Microanal. Microstruct. **3**, 363 (1992).
[20] R. Balboni, S. Frabboni, and A. Armigliato, Philos. Mag. A **77**, 67 (1998).
[21] A. Armigliato, R. Balboni, I. De Wolf, S. Frabboni, K. G. F. Janssens, and J. Vanhellemont, Inst. Phys. Conf. Ser. **134**, 229 (1993).
[22] J. Vanhellemont, I. De Wolf, K. G. F. Janssens, S. Frabboni, R. Balboni, and A. Armigliato, Appl. Surf. Sci. **63**, 119 (1993).
[23] J. Vanhellemont, K. G. F. Janssens, S. Frabboni, P. Smeys, R. Balboni, and A. Armigliato, Mater. Res. Soc. Symp. Proc. **405**, 435 (1996).
[24] C. Stuer, J. Van Landuyt, H. Bender, I. De Wolf, R. Rooyackers, and G. Badenes, J. Electrochem. Soc. **148**, 597 (2001).
[25] A. Armigliato, R. Balboni, S. Frabboni, A. Benedetti, A. G. Cullis, G. P. Carnevale, P. Colpani, and G. Pavia, Mater. Sci. Semicond. Process. **4**, 97 (2001).
[26] A. Armigliato, R. Balboni, S. Frabboni, A. Benedetti, A. G. Cullis, and G. Pavia, Inst. Phys. Conf. Ser. **169**, 467 (2001).
[27] A. Toda, N. Ikarashi, H. Ono, and K. Okonogi, Appl. Phys. Lett. **80**, 2278 (2002).
[28] H. K. Gummel, IEEE Trans. Electron Devices **11**, 455 (1964).
[29] D. Scharfetter and H. K. Gummel, IEEE Trans. Electron Devices **16**, 64 (1969).
[30] B. E. Deal and A. S. Grove, J. Appl. Phys. **36**, 3770 (1965).
[31] P. E. Cottrell and E. M. Buturla, Tech. Dig. - Int. Electron Devices Meet. **1975**, 51.
[32] S. Selberherr, A. Schutz, and W. Potzl, IEEE Trans. Electron Devices **27**, 1540 (1980).
[33] D. A. Antoniadis, S. E. Hansen, and R. W. Dutton, Technical Report No. 5019-2, Standford Electronics Laboratory (1978).
[34] W. G. Oldham, S. Nandgaonkar, A. R. Neureuther, and M. O. Toole, IEEE Trans. Electron Devices **26**, 717 (1979).
[35] K. Taniguchi, M. Kashiwagi, and H. Iwai, IEEE Trans. Electron Devices **28**, 574 (1981).
[36] R. B. Penumalli, IEEE Trans. Electron Devices **30**, 986 (1983).
[37] L. Borucki, H. Hansen, and K. Varahramyan, IBM J. Res. Dev. **29**, 263 (1985).
[38] J. Lorenz, J. Pelka, H. Ryssel, A. Sachs, A. Seidl, and M. Svoboda, IEEE Trans. Comput.-Aided Des. **4**, 10 (1985).
[39] B. Baccus, E. Dubois, D. Collard, and D. Morel, Solid-State Electron. **32**, 1013 (1989).
[40] S. K. Jones, C. Lombardi, A. Poncet, C. Hill, H. Jaouen, J. Lorenz, C. Lyden, K. De Meyer, J. Pelka, M. Rudan, and S. Solmi, Proceedings of the ESSDERC'93 (1993), p. 505.
[41] S. Odanaka, H. Umimoto, M. Wakabayashi, and H. Esaki, IEEE Trans. Comput.-Aided Des. **7**, 675 (1988).
[42] S. Ushio, K. Nishi, S. Kuroda, K. Kai, and J. Ueda, IEEE Trans. Comput.-Aided Des. **9**, 41 (1990).
[43] G. Baccarani, P. Ciampolini, and A. Pierantoni, Nucl. Instrum. Methods Phys. Res. A **326**, 253 (1993).
[44] V. Senez, S. Bozek, and B. Baccus, Tech. Dig. - Int. Electron Devices Meet. **1996**, 705.
[45] J. Vanhellemont, S. Amelinckx, and C. Claeys, J. Appl. Phys. **61**, 2170 (1987).
[46] S. M. Hu, J. Appl. Phys. **70**, R53 (1991).
[47] P. M. Fahey, S. R. Mader, S. R. Stiffler, R. L. Mohler, J. D. Mis, and J. A. Slinkman, IBM J. Res. Dev. **36**, 158 (1992).
[48] D. Chin, S. H. Oh, and R. W. Dutton, IEEE Trans. Electron Devices **30**, 993 (1983).
[49] A. Poncet, IEEE Trans. Comput.-Aided Des. **4**, 41 (1985).
[50] M. J. Needs, V. Jovic, C. Taylor, K. Board, and M. J. Cooke, Proceedings of the SISDEP'86, Swansea (1986).
[51] S. Isomae and S. Yamamoto, IEEE Trans. Comput.-Aided Des. **6**, 410 (1987).
[52] P. Sutardja and W. G. Oldham, IEEE Trans. Electron Devices **36**, 2415 (1989).
[53] H. Umimoto, S. Odanaka, I. Nakao, and H. Esaki, IEEE Trans. Comput.-Aided Des. **8**, 599 (1989).
[54] S. T. Ahn, H. W. Kennel, J. D. Plummer, and W. A. Tiller, J. Appl. Phys. **64**, 4914 (1988).
[55] H. Park, K. S. Jones, J. A. Slinkman, and M. E. Law, Tech. Dig. - Int. Electron Devices Meet. **1993**, 303.
[56] K. Osada, S. Matsumoto, M. Yoshida, and E. Arai, in *Proceedings of the Third International Symposium on Process Physics and Modeling in Semiconductor Technology* (Electrochemical Society, New York, 1993), p. 98.
[57] H. Miura, N. Saito, and N. Okamoto, Proceedings of SISDEP 1993 (1993), p. 177.
[58] P. Ferreira, V. Senez, and B. Baccus, IEEE Trans. Electron Devices **43**, 1525 (1996).
[59] P. B. Griffin and C. S. Rafferty, Tech. Dig. - Int. Electron Devices Meet. **1990**, 741.
[60] T. Kuroi, Y. Uchida, K. Horita, M. Sakai, Y. Itoh, Y. Inoue, and T. Nishimura, Tech. Dig. - Int. Electron Devices Meet. **1998**, 141.
[61] M. Nandakumar, A. Chatterjee, S. Sridhar, K. Joyner, M. Rodder, and I. C. Chen, Tech. Dig. - Int. Electron Devices Meet. **1998**, 133.
[62] P. Ambree, F. Kreller, R. Wolf, and K. Wandel, J. Vac. Sci. Technol. B **11**, 614 (1993).
[63] A. Goullet, C. Vallee, A. Granier, and G. Turban, J. Vac. Sci. Technol. A **18**, 2452 (2000).
[64] I. De Wolf, H. E. Maes, and S. K. Jones, J. Appl. Phys. **79**, 7148 (1996); I. De Wolf and E. Anastassakis, *ibid.* **85**, 7484 (1999).
[65] P. M. Jones, G. M. Rackham, and J. W. Steeds, Proc. R. Soc. London, Ser. A **354**, 197 (1977).

[66] A. Benedetti, A. G. Cullis, A. Armigliato, R. Balboni, S. Frabboni, G. F. Mastracchio, and G. Pavia, Appl. Surf. Sci. **188**, 214 (2002).
[67] V. Senez, D. Collard, B. Baccus, M. Brault, and J. Lebailly, J. Appl. Phys. **76**, 3285 (1994).
[68] V. Senez, T. Hoffmann, P. Le Duc, and F. Murray, J. Appl. Phys. **93**, 6039 (2003).
[69] P. Ferreira, V. Senez, and B. Baccus, IEEE Trans. Electron Devices **43**, 1525 (1995).
[70] T. Hoffmann, P. Le Duc, and V. Senez, J. Vac. Sci. Technol. B **17**, 2603 (1999).
[71] V. Senez, T. Hoffmann, and A. Tixier, IEEE Trans. Semicond. Manuf. **13**, 416 (2000).
[72] R. von Mises, Z. Angew. Math. Mech. **8**, 161 (1928).
[73] A. Nadai, *Theory of Flow and Fracture of Solids* (McGraw-Hill, New York, 1950).
[74] R. Dwa, Z. Angew. Math. Mech. **79**, 281 (1999).